Optimal Solar Sail Transfers Between Halo Orbits of Different Sun-Planet Systems

Jeannette Heiligers,[†] Giorgio Mingotti, and Colin R. McInnes

Advanced Space Concepts Laboratory, Department of Mechanical & Aerospace Engineering, University of Strathclyde, 75 Montrose Street, G1 1XJ Glasgow, U.K

Abstract

This paper investigates time-optimal solar sail trajectories between Libration Point Orbits (LPOs) of different circular restricted Sun-planet three-body systems. Key in the investigations is the search for transfers that require little steering effort to enable the transfers with low-control authority solar sail-like devices such as SpaceChips. Two transfers are considered: 1) from a Sun-Earth L_2-Halo orbit to a Sun-Mars L_1-Halo orbit and 2) from a Sun-Earth L_1-Halo orbit to a Sun-Mercury L_2-Halo orbit. The optimal control problem to find these time-optimal transfers is derived, including a constraint to mimic limited steering capabilities, and is solved with a direct pseudospectral method for which novel first guess solutions are developed. For a near-term sail performance comparable to that of NASA's Sunjammer sail, the results show transfers that indeed require very little steering effort: the sail acceleration vector can be bounded to a cone around the Sun-sail line with a half-angle of 7.5 deg. These transfers can serve a range of novel solar sail applications covering the entire spectrum of sail length-scales: micro-sized SpaceChips could establish a continuous Earth-Mars communication link, a traditional-sized sail provides opportunities for in-situ observations of Mercury and a future kilometer-sized sail could create an Earth-Mars cargo transport gateway for human exploration of Mars.

Keywords: Solar sailing; Trajectory Optimisation; Heteroclinic Connections; Circular Restricted Three-Body Problem; Libration Point Orbits.

---

[*] Part of the work described in this paper has been presented at the 2nd IAA Conference on Dynamics and Control of Space Systems - DyCoSS 2014, Rome, Italy, 24-26 March 2014.

[†] Corresponding author. Email address: jeannette.heiligers@strath.ac.uk. Phone: +44 141 141 574 5989

1. Introduction

Research in the field of solar sailing is flourishing, sparked by successes such as JAXA's IKAROS mission (Tsuda et al., 2011) and new solar sail initiatives including NASA's Sunjammer mission[*]. Its potential lies in the fact that solar sail missions are not constrained by a propellant mass (McInnes, 1999). By using the Sun as "propellant source", solar sails obtain their propulsive acceleration by reflecting photons off a highly reflective membrane. This gives solar sails a theoretically unlimited lifetime and enables a wealth of novel orbits and space applications, including displaced geostationary orbits to create additional geostationary slots for telecommunication, Earth observation and weather satellites (Heiligers et al., 2011, Baig and McInnes, 2010) and orbits displaced below the lunar south pole (Wawrzyniak and Howell, 2011) or above the Earth-Moon L_2 point (McInnes, 1993) to establish an Earth-Moon communications link.

Instead of investigating the set of novel orbits that solar sails enable, this paper focusses on their transfer capabilities, in particular in the circular restricted three body problem (CR3BP). Solar sail transfers in the CR3BP have been investigated before, for example to fly out to periodic orbits around Sun-Earth Lagrange points (also referred to as Libration Point Orbits (LPOs)) (Heiligers et al., 2012) and to move between artificial equilibrium points in the Sun-Earth system (Heiligers and McInnes, 2013). However, solar sail transfers between LPOs in different Sun-planet systems have so-far not been investigated, despite the fact that they offer great potential for additional novel space applications. Note that these types of interplanetary connections have been the topic of a limited number of papers (Pergola et al., 2009, Mingotti et al., 2011, Topputo et al., 2005), but all considered either the use of an impulsive maneuver or solar electric propulsion to establish the connection, while this paper demonstrates the capabilities of solar sailing.

For the purpose of demonstrating the concept's feasibility, this paper investigates two particular solar sail transfers: 1) the transfer from a Sun-Earth L_2-Halo orbit to a Sun-Mars L_1-Halo orbit and 2) the transfer from a Sun-Earth L_1-Halo orbit to a Sun-Mercury L_2-Halo orbit. Note that, for brevity, the remainder of this paper will refer to these orbits as Earth-L_2, Mars-L_1, Earth-L_1 and Mercury-L_2 Halo orbits, respectively. For both cases the time-optimal transfer will be sought for by solving the accompanying optimal control problem with a direct pseudospectral method. Note

[*] L'Garde Inc., L'Garde - Sunjammer, http://www.lgarde.com/programs/space-propulsion/sunjammer, Accessed 8 May 2013.

that, while solar sail displaced LPOs exist (Baoyin and McInnes, 2006), this work only considers the transfer between LPOs in the classical CR3BP. The solar sail acceleration is thus only employed to leave the initial Halo orbit and to transfer towards and wind onto the target Halo orbit.

Another novelty introduced in this paper is the consideration of low-control authority solar sails that can change their attitude only to a limited extent. The reason for investigating this scenario is the development of so-called SpaceChips: miniturised operational spacecraft of a few centimeters in size. With a high area-to-mass ratio, these devices act as solar sails and with low production costs and low mass they enable a range of new space applications (Colombo et al., 2012). However, they will have limited steering capabilities. Constraints on the control authority of solar sails have been investigated before. For example, (Mengali and Quarta, 2014) found time-optimal Earth-Mars orbital rendezvous missions after fixing the cone angle. However, with still full control over the clock angle and relatively large (constant) cone angles, significant control authority can still be achieved. Instead, in this work the authors show that, even with extremely low-control authority, feasible and relatively quick transfers can be accomplished.

For comparison and to highlight the different applications of the transfers, this paper will consider both high-control authority traditional solar sails as well as control-limited SpaceChips. Distributing micro-sized (10^{-2} m), low-control authority SpaceChips along a trajectory connecting an Earth-L_2 Halo orbit with a Mars-L_1 Halo orbit establishes a continuous Earth-Mars communication link, even during Martian occultation; alternatively, a meso-sized (10-100 m), fully steerable solar sail can enable an interesting planetary observation platform at Mercury through the use of a connection between Earth-L_1 and Mercury-L_2; and finally, in the macro-scale (10^3 m), the previously mentioned Earth-Mars link allows a vital gateway for cargo transport for future human exploration on Mars.

The structure of the paper will be as follows. First, the dynamical model will be explained: the classical circular restricted three body problem will be revisited and a solar sail acceleration will be added. To include fourth-body perturbations the ephemerides employed will be described and the required reference frame transformations will be discussed. Finally, the LPOs considered in this paper will be derived and presented. The second part of the paper will focus on the definition of the optimal control problem. Since the start and end points of the transfer are defined in different CR3BPs, a two phased approach will be introduced. The required phase-linkage constraints, boundary constraints and path constraints will be discussed. The latter include the important constraint on the steering capability of the solar sail in order to mimic the low-control authority of

SpaceChips. Subsequently, the development of novel first guesses for the transfers under consideration will be discussed. The last part of the paper will present the optimal results for both the Earth-to-Mars and Earth-to-Mercury transfers and the paper will end with the conclusions.

2. Dynamical model

2.1 Circular restricted three-body problem

The dynamic model employed in this paper is the well-known circular restricted three-body problem (CR3BP), which describes the motion of an infinitely small mass, m, (here the solar sail) under the influence of the gravitational attraction of two much larger masses, m_1 and m_2, also referred to as the primaries. The gravitational influence of the small mass on the primaries is neglected and the primaries are assumed to move in circular orbits about their common centre-of-mass (Battin, 1999).

The reference frame employed is a synodic reference frame and is depicted in Figure 1a: the origin coincides with the barycentre of the system, the x-axis connects m_1 and m_2 and points in the direction of m_2, the z-axis is directed perpendicular to the plane in which m_1 and m_2 orbit and the y-axis completes the right-handed reference frame. Finally, the frame rotates at constant angular velocity, ω, around the z-axis: $\boldsymbol{\omega} = \omega\hat{\mathbf{z}}$.

New units are introduced in the CR3BP: the sum of the two larger masses is taken as the unit of mass, i.e. $m_1 + m_2 = 1$. Then, with the mass ratio $\mu = m_2/(m_1 + m_2)$, the masses of the primaries become $m_1 = 1-\mu$ and $m_2 = \mu$. As unit of length, λ, the distance between the primaries is selected, and $1/\omega$ is chosen as unit of time, τ, yielding $\omega = 1$, and so one orbital period of the planet around the Sun is represented by 2π. Three different CR3BPs will be employed throughout this work: Sun-Earth, Sun-Mars and Sun-Mercury. Parameters for each of the CR3BPs are provided in Table 1.

The motion of a solar sail in any of the CR3BPs is governed by the following equations of motion (McInnes, 1999):

$$\ddot{\mathbf{r}} + 2\boldsymbol{\omega}\times\dot{\mathbf{r}} + \boldsymbol{\omega}\times(\boldsymbol{\omega}\times\mathbf{r}) + \nabla V = \mathbf{a}_s + \mathbf{a}_4 \tag{1}$$

with V the gravitational potential and nearly all other definitions provided in Figure 1a. The left hand side of Eq. (1) describes the classical (i.e. ballistic) CR3BP, while the right hand side adds

two perturbing terms: the solar sail acceleration, $\mathbf{a}_s$, and the fourth-body perturbation $\mathbf{a}_4$, which will be discussed in the next two subsections.

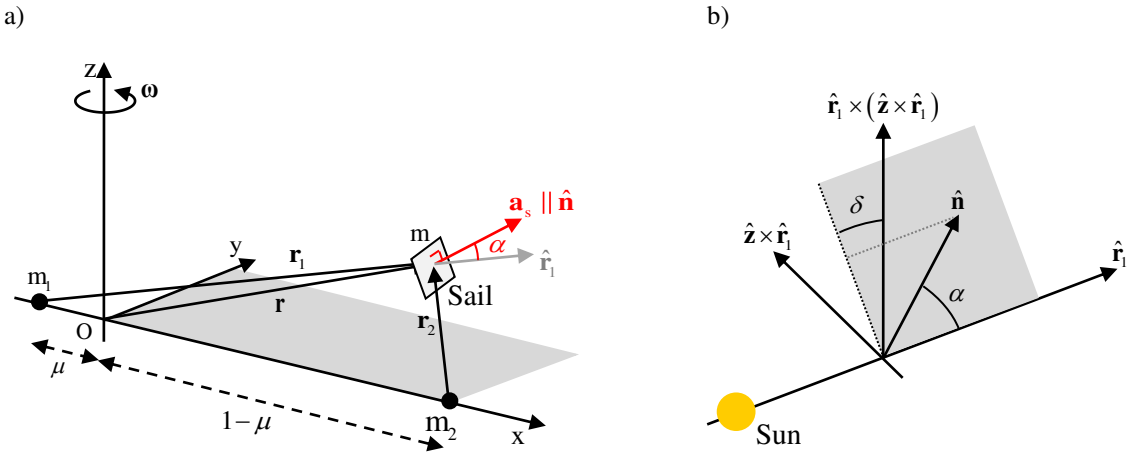

Figure 1 a) Schematic of circular restricted three-body problem. b) Definition of solar sail normal vector.

Table 1 Circular restricted three-body problem parameters

CR3BP	μ	λ	τ	μ_4
Sun-Earth	3.0034599e-6	1.4947600e9	5.0162789e6	Mercury: 1.6601428e-7 Mars: 3.2268266e-7
Sun-Mars	3.2268352e-7	2.2793910e9	9.4461038e6	Earth: 3.0034679e-6
Sun-Mercury	1.6601475e-7	5.7909100e7	1.2096630e6	Earth: 3.0034684e-6

2.2 Solar sail acceleration

An ideal solar sail model is adopted, which assumes pure specular reflection of the impinging photons (McInnes, 1999). The solar sail acceleration vector then acts normal to the solar sail surface, i.e. in direction $\hat{\mathbf{n}}$, and is defined as:

$$\mathbf{a}_s = a_s \hat{\mathbf{n}} = \beta \frac{1-\mu}{r_1^2} \left(\hat{\mathbf{r}}_1 \cdot \hat{\mathbf{n}}\right)^2 \hat{\mathbf{n}} \tag{2}$$

The attitude of the solar sail can be expressed through two angles, the cone angle, α, and the clock angle, δ, see Figure 1b. From Eq. (2) it is clear that the sail acceleration magnitude is pro-

portional to the solar gravitational acceleration, $(1-\mu)/r_1^2$, and is scaled by the sail lightness number, β. The lightness number can be expressed as a function of the sail area to spacecraft mass ratio, σ, and the critical solar sail loading parameter, $\sigma^* = 1.53$ g/m^2 (McInnes, 1999):

$$\beta = \frac{\sigma^*}{\sigma} \tag{3}$$

A realistic near-term value for the lightness number can be derived from the expected lightness number of the Sunjammer mission, which is scheduled for launch post-2015. The Sunjammer solar sail was designed to be 38 x 38 m^2 in size with a mass estimate of about 45 kg (Heiligers et al., 2014). In an ideal case, this results in a lightness number of 0.0491, which for convenience will be round in this work to a value of $\beta = 0.05$. Another common parameter to express the performance of a solar sail is the characteristic acceleration, which is defined as the acceleration produced by a Sun-facing solar sail at Earth's distance. A sail lightness number of 0.05 then corresponds to a characteristic acceleration $a_c = \beta \frac{\mu_S}{AU^2} = 0.3$ mm/s^2 with μ_S the gravitational parameter of the Sun and AU the astronomical unit.

Finally, Eq. (2) takes into account the reduced projected solar sail area when the sail is pitched at a cone angle, $\alpha = \cos^{-1}(\hat{\mathbf{r}}_1 \cdot \hat{\mathbf{n}})$, with respect to the Sun-sail line through the term $(\hat{\mathbf{r}}_1 \cdot \hat{\mathbf{n}})^2$.

2.3 Fourth-body perturbation

As became clear in the introduction, the starting LPO and target LPO are defined in different CR3BPs. The first and second sections of the transfer connecting these LPOs will therefore also be defined in different CR3BPs. In order for the dynamics to be consistent throughout the transfer, a fourth-body perturbation is included. For example, for the Earth-L_2 to Mars-L_1 transfer, Mars will be the fourth-body in the first part of the transfer, i.e. in the Sun-Earth CR3BP, while the Earth will be the fourth-body in the second part of the transfer, i.e. in the Sun-Mars CR3BP.

The perturbing acceleration, $\mathbf{a}_4$, is defined as:

$$\mathbf{a}_4 = \frac{\partial \Omega_4}{\partial \mathbf{r}}, \quad \Omega_4 = \mu_4 \left(\frac{1}{|\mathbf{r}_{s,4}|} - \frac{\mathbf{r} \cdot \mathbf{r}_4}{|\mathbf{r}_4|} \right) \tag{4}$$

with $\mu_4 = m_4/(m_1 + m_2)$ and m_4 the mass of the fourth-body, see Table 1 for values. All other variables in Eq. (4) are defined in Figure 2.

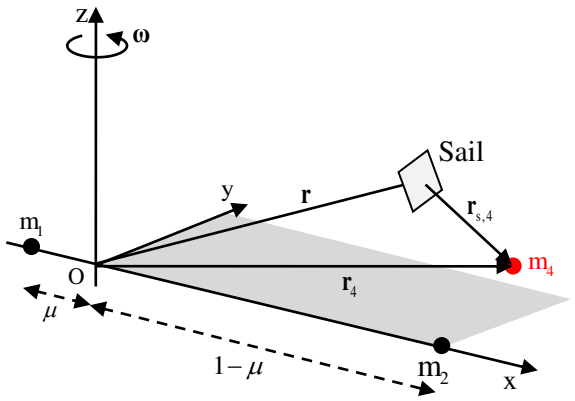

Figure 2 Fourth-body perturbation geometry.

2.4 Ephemerides

The inclusion of the fourth-body perturbation transforms the autonomous CR3BP into a non-autonomous problem. The actual relative position of the planets thus comes into play and is calculated using the analytical ephemerides implemented in the Matlab® function uplanet.m (Dysli, 1977) that was successfully verified against the JPL/NAIF/SPICE DE405 ephemerides. This function describes the ephemerides in an inertial heliocentric reference frame: the $\tilde{x}$-axis points towards the vernal equinox, the $\tilde{z}$-axis is perpendicular to the ecliptic plane and the $\tilde{y}$-axis completes the right-handed reference frame, see Figure 4.

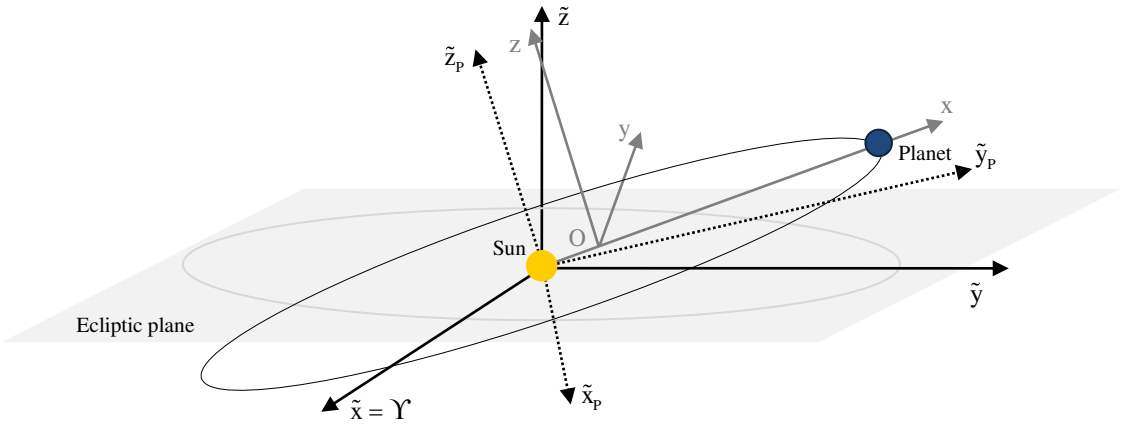

Figure 3 Schematic of heliocentric inertial reference frames, $(\tilde{x}, \tilde{y}, \tilde{z})$ and $(\tilde{x}_P, \tilde{y}_P, \tilde{z}_P)$, and Sun-planet synodic reference frame, (x, y, z).

2.5 Reference frame transformations

Since the ephemeris of the planets are provided in an heliocentric inertial reference frame, a transformation is required to obtain the planet's state vector in the Sun-planet synodic reference frame for use in Eq. (4).

First, a state vector $\tilde{\mathbf{x}} = \left[\tilde{\mathbf{r}} \quad \dot{\tilde{\mathbf{r}}}\right]^T$ in the heliocentric inertial reference frame is transformed to an intermediate, different heliocentric inertial reference frame, $\left(\tilde{x}_P, \tilde{y}_P, \tilde{z}_P\right)$, where the $\tilde{x}_P$-axis points along the planet's line of nodes, the $\tilde{z}_P$-axis is perpendicular to the planet's orbital plane and the $\tilde{y}_P$-axis completes the right-handed reference frame, see Figure 4. The state vector in this new inertial reference frame $\tilde{\mathbf{x}}_P = \left[\tilde{\mathbf{r}}_P \quad \dot{\tilde{\mathbf{r}}}_P\right]^T$ is:

$$\tilde{\mathbf{x}}_P = \mathbf{R}_x(-i)\mathbf{R}_z(-\Omega)\tilde{\mathbf{x}} \tag{5}$$

with $\mathbf{R}_x$ and $\mathbf{R}_z$ rotation matrices around the $x-$ and $z-$axes and i and Ω the inclination and right ascension of the ascending node of the planet's orbital plane, respectively. Note that for the Earth, the two heliocentric inertial reference frames coincide. Subsequently, the state vector in the Sun-planet synodic reference frame, $\mathbf{x} = \left[\mathbf{r} \quad \dot{\mathbf{r}}\right]^T$, can be computed using:

$$\begin{aligned} \mathbf{r} &= \mathbf{R}_z(-u)\tilde{\mathbf{r}}_P - \left[\mu \quad 0 \quad 0\right]^T \\ \dot{\mathbf{r}} &= \mathbf{R}_z(-u)\dot{\tilde{\mathbf{r}}}_P - \boldsymbol{\omega} \times \left(\mathbf{R}_z(-u)\tilde{\mathbf{r}}_P\right) \end{aligned} \tag{6}$$

with u the planet's argument of latitude. In Eq. (6) the rotation matrix $\mathbf{R}_z$ rotates the $\tilde{x}_P$-axis onto the x-axis, translates the origin of the reference frame from the Sun to the barycenter and accounts for the rotational velocity of the synodic reference frame.

A simple relationship also exists between the dimensional time $\tilde{t}_{MJD2000}$ in the heliocentric inertial reference frame and the dimensionless time t in the Sun-planet synodic reference frame. By defining $t = \tilde{t}_{MJD2000} = 0$ to be 1-1-2000, $t = 2\pi$ corresponds to $\tilde{t}_{MJD2000} = 2\pi/\tau$, or equivalently: 1-1-2001 in the Sun-Earth problem, 18-11-2001 in the Sun-Mars problem and 29-3-2000 in the Sun-Mercury problem.

2.6 Lagrange Point Orbits

As discussed, when discarding the solar sail and fourth-body perturbation accelerations in Eq. (1), the classical CR3BP is obtained. This problem generates five equilibrium solutions, or Lagrange points, by setting the time derivatives of the position vector equal to zero, i.e. $\ddot{\mathbf{r}} = \dot{\mathbf{r}} = 0$.

The two Lagrange points considered in this work are the collinear L_1 (between m_1 and m_2) and L_2 (behind m_2) points. It is well-known that a range of periodic orbits can be found around these Lagrange points. Here the family of Halo orbits is considered, which can be generated following (Howell, 1983). Four particular Halo orbits are selected, one around Earth-L_1, one around Earth-L_2, one around Mars-L_1 and one around Mercury-L_2. While the first three are northern Halo orbits, the Halo orbit around Mercury-L_2 is a southern Halo orbit. The projections onto the ecliptic and out-of-ecliptic plane for each of the Halo orbits are given in Figure 4, while Table 2 gives further details. Note that the Halo orbits in Figure 4 can be generated by simply forward integrating the initial conditions $\mathbf{x}_0 = [\mathbf{r}_0 \quad \dot{\mathbf{r}}_0]^T$ provided in Table 2 in Eq. (1) with $\mathbf{a}_s = \mathbf{a}_4 = \mathbf{0}$.

Table 2 Details of Halo orbits with $\mathbf{r}_0$ and $\dot{\mathbf{r}}_0$ the initial position and velocity vector and P_{LPO} the orbital period. Note that all variables are made dimensionless with respect to the respective CR3BP.

Halo orbit	$[\mathbf{r}_0 \quad \dot{\mathbf{r}}_0]^T$	P_{LPO}
Earth-L_2	$[1.0068 \quad 0 \quad -0.0035683 \quad 0 \quad 0.014705 \quad 0]^T$	3.0741
Mars-L_1	$[0.99477 \quad 0 \quad -0.0016975 \quad 0 \quad 0.004996 \quad 0]^T$	3.0602
Earth-L_1	$[0.9892 \quad 0 \quad -0.0048992 \quad 0 \quad 0.011603 \quad 0]^T$	3.0388
Mars-L_2	$[1.0025 \quad 0 \quad 0.0014694 \quad 0 \quad 0.0059461 \quad 0]^T$	3.0555

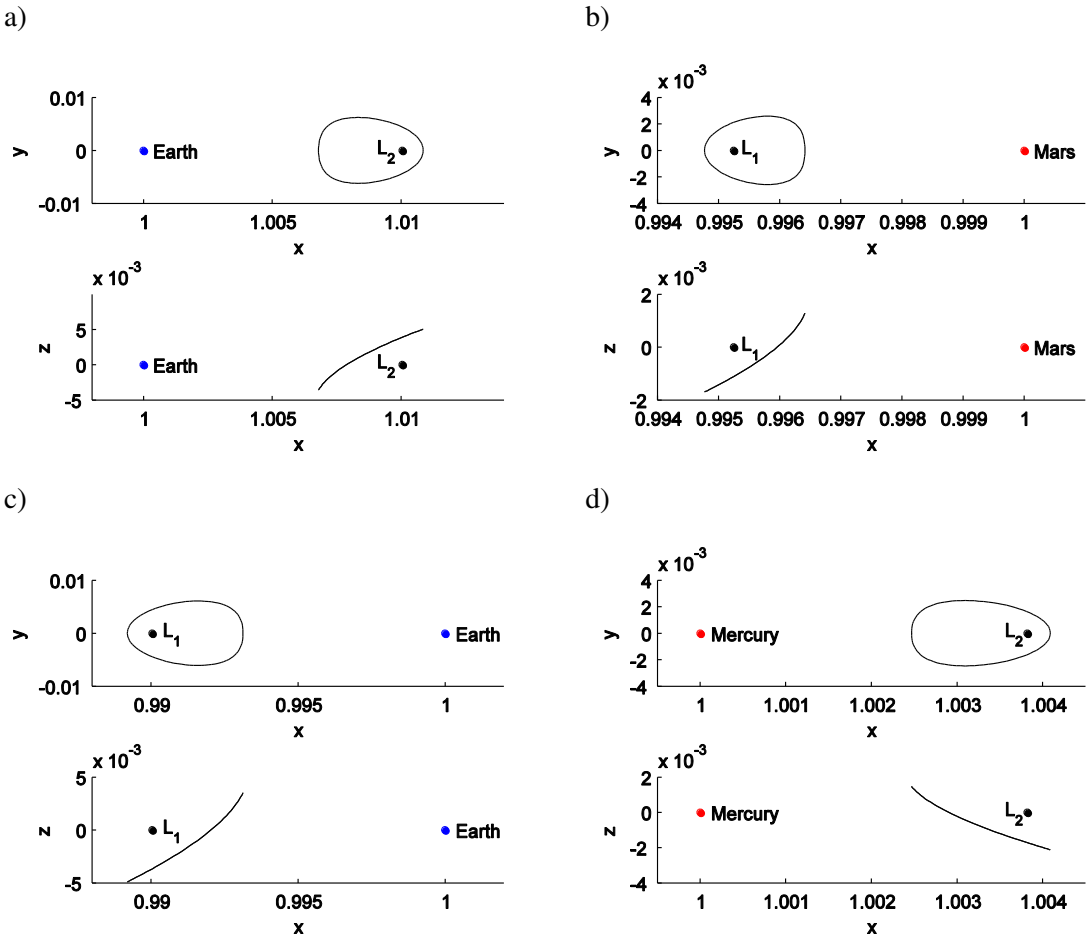

Figure 4 Projections of Halo orbits around: a) Northern Halo at Earth-L_2 b) Northern Halo at Mars-L_1 c) Northern Halo at Earth-L_1 and d) Southern Halo at Mercury-L_2.

3. Optimisation problem

With the initial and target LPOs defined, the problem now becomes to find optimal solar sail transfers between these LPOs. In particular between Earth-L_2 and Mars-L_1 and between Earth-L_1 and Mercury-L_2

In general, an optimal control problem can be defined as finding a state history $\mathbf{x}(t) \in \mathbb{R}^{n_x}$ and a control history $\mathbf{u}(t) \in \mathbb{R}^{n_u}$ with $t \in [t_0, t_f]$ the independent variable, that minimises a cost function, J. In this work, the cost function is the time of flight:

$$J = t_f - t_0 \tag{7}$$

where the subscripts 0 and f indicate the initial and final conditions, respectively.

The state history consists of the Cartesian position and velocity components in the Sun-planet synodic reference frame of Figure 1:

$$\mathbf{x} = \begin{bmatrix} x & y & z & \dot{x} & \dot{y} & \dot{z} \end{bmatrix}^T \tag{8}$$

where the time dependency due to the fourth-body perturbation is omitted from the notation for brevity and appropriate bounds on these Cartesian position and velocity components are selected for each of the cases considered.

The control history consists of the Cartesian components of the normal vector to the solar sail (or equivalently the unit solar sail acceleration vector):

$$\begin{bmatrix} -1 & -1 & -1 \end{bmatrix}^T \leq \mathbf{u} = \begin{bmatrix} n_x & n_y & n_z \end{bmatrix}^T \leq \begin{bmatrix} 1 & 1 & 1 \end{bmatrix}^T \tag{9}$$

Finally, the independent variable is the dimensionless time, t. Bounds on the initial and final time are imposed such that a 2020-2025 launch window and a 2020-2027 arrival window are ensured. In dimensionless time, these windows translate into:

$$\begin{array}{ll} 40\pi \leq t_{0,} \leq 50\pi & \text{Sun-Earth system} \\ 21.2\pi \leq t_f \leq 28.8\pi & \text{Sun-Mars system} \\ 166.1\pi \leq t_f \leq 224.2\pi & \text{Sun-Mercury system} \end{array} \tag{10}$$

3.1 Two-phase approach

As indicated before, due to the fact that the initial and target LPOs are defined in different CR3BPs, the initial and final parts of the transfer will also have to be defined in different CR3BPs. The transfer is therefore split into two phases, where the first phase (hereafter referred to through the subscript p_1) is defined in the Sun-Earth CR3BP with either Mars of Mercury as fourth-body, while the second phase (referred to through the subscript p_2) is defined in the Sun-Mars/Mercury CR3BP with Earth as fourth-body, see also Figure 5.

Clearly, a smooth linkage between the two phases has to exist, i.e. a smooth linkage between the final conditions of the first phase and the initial conditions of the second phase. Therefore, constraints are enforced that guarantee continuity across the linkage in terms of position, velocity, time and sail attitude. Since two different CR3BPs are linked, the relative orientation of the synodic reference frames at the time of the linkage needs to be considered. Therefore, the reverse of the transformation described in Eqs. (5)-(6) is used to transform the final state vector of the first

phase, $\mathbf{x}_{f,p_1}$, and the initial state vector of the second phase, $\mathbf{x}_{0,p_2}$, to the heliocentric inertial reference frame. In this reference frame, the two state vectors can be equated to ensure a continuous link between the two phases:

$$\tilde{\mathbf{x}}_{f,p_1} = \tilde{\mathbf{x}}_{0,p_2} \tag{11}$$

A similar transformation is performed to obtain a continuous link on the sail attitude such that the following constraint can be enforced:

$$\tilde{\mathbf{u}}_{f,p_1} = \tilde{\mathbf{u}}_{0,p_2} \tag{12}$$

Finally, the dimensionless time is converted to dimensional time $\tilde{t}_{MJD2000}$ to also guarantee a continuous link in terms of time:

$$\tilde{\tilde{t}}_{MJD2000,f,p_1} = \tilde{t}_{MJD2000,0,p_2} \tag{13}$$

From Eqs. (11)-(13) it is clear that, in total, 10 linkage constraints are enforced.

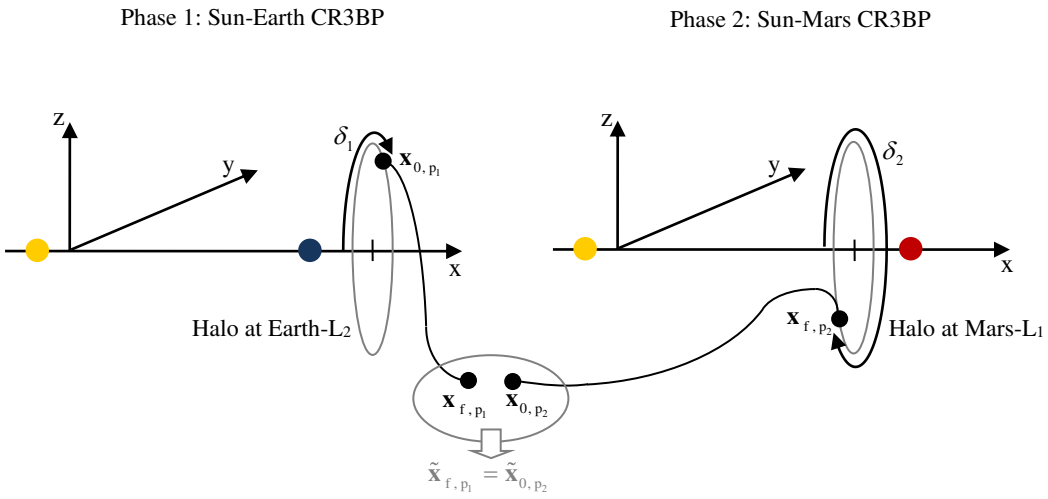

Figure 5 Illustration of two-phase approach for the Earth-L_2 to Mars-L_1 transfer and definition of static optimisation parameters δ_1 and δ_2.

3.2 Boundary constraints

To ensure that the trajectory departs from the Earth L_2/L_1 LPO and winds onto the Mars-L_1 or Mercury-L_2 LPO, a set of boundary constraints are imposed: the state vector at the start of phase 1, $\mathbf{x}_{0,p_1}$, should coincide with the Earth L_2/L_1 LPO and the state vector at the end of phase 2, $\mathbf{x}_{f,p_2}$, should coincide with the Mars-L_1 or Mercury-L_2 LPO. The values of two static optimisation parameters, δ_1 and δ_2, are optimised simultaneously with the rest of the optimal control problem to find the best departure and arrival conditions on these LPOs. These static parameters define a sampling of the LPOs and are defined as $0 \le \delta_1 \le P_{LPO,p_1}$ and $0 \le \delta_2 \le P_{LPO,p_2}$, see also Figure 5 and Table 2 for values. The boundary constraints thus become:

$$\mathbf{x}_{0,p_1} = \mathbf{x}_{LPO,p_1}(\delta_1) \tag{14}$$

$$\mathbf{x}_{f,p_2} = \mathbf{x}_{LPO,p_2}(\delta_2) \tag{15}$$

The actual values for $\mathbf{x}_{LPO,p_1}(\delta_1)$ and $\mathbf{x}_{LPO,p_2}(\delta_2)$ are computed through an interpolation of large state matrices that provide the position and velocity vectors along the LPOs on a 100-grid point mesh in δ_1 or δ_2, i.e. for a discrete number of locations along each of the LPOs.

Note that no boundary constraints are imposed on the final conditions of the first phase and the initial conditions of the second phase. The choice for the location and time of the linkage as defined in Eqs. (11) and (13) are thus completely free and optimisable.

Finally, also note that the departure and arrival orbits do not incorporate a solar sail acceleration. The sail therefore has to be 'switch on' or deployed upon departure from the Earth L_2/L_1 Halo orbit and 'switched off' or ejected upon arrival at the Mars-L_1 or Mercury-L_2 Halo orbit. For low-control authority solar sails such as SpaceChips deployment or ejection may not be possible and an attitude change will be required to ensure that the SpaceChips are positioned edgewise to the Sun when orbiting the ballistic Halo orbits. In future work, this control effort may be traded off against the time of flight to find alternative optimal values for δ_1 and δ_2.

3.3 Path constraints

A set of path constraints are enforced on the control vector that will hold throughout the entire trajectory, i.e. in both phases 1 and 2. First, a path constraint is introduced to ensure that the norm of the control vector is unity:

$$|\mathbf{u}| = 1 \tag{16}$$

A second path constraint makes sure that the control vector always points away from the Sun. This has to be taken into account because a solar sail cannot generate an acceleration component in the direction of the Sun (McInnes, 1999):

$$\hat{\mathbf{r}}_l \cdot \hat{\mathbf{n}} \geq 0 \tag{17}$$

A final path constraint is defined to introduce limitations on the control authority of the solar sail as discussed in the introduction of this paper. This is done by defining two more static optimisation parameters, $0 \leq \alpha_{ref} \leq \frac{1}{2}\pi$ and $0 \leq \delta_{ref} \leq 2\pi$ that describe a constant cone and clock angle to define an optimal solar sail reference attitude, $\hat{\mathbf{n}}_{ref}$, see Figure 1b for the definition of the cone and clock angles. To limit the control authority of the solar sail, the solar sail acceleration unit vector, $\hat{\mathbf{n}}$, is now allowed to move within a cone around $\hat{\mathbf{n}}_{ref}$ with a half-cone angle $\Delta\alpha$, see Figure 6. The value for $\Delta\alpha$ is an input parameter of the optimal control problem. The associated path constraint then becomes:

$$\cos^{-1}\left(\hat{\mathbf{n}}_{ref} \cdot \hat{\mathbf{n}}\right) \leq \Delta\alpha \tag{18}$$

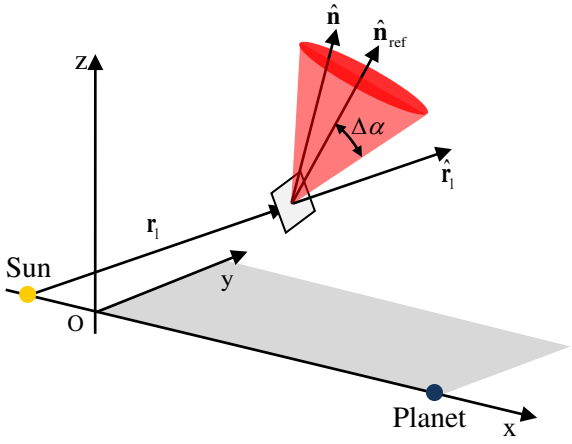

Figure 6 Illustration of solar sail limited control authority.

3.4 Optimal control solver

The optimal control problem defined in the previous sections is solved with a direct pseudospectral method, which discretises the time interval into a finite number of collocation points and uses Legendre or Chebyshev polynomials to approximate and interpolate the time dependent variables at the collocation points. This way, the infinite dimensional optimal control problem is transformed into a finite dimension non-linear programming (NLP) problem. Pseudospectral methods have gained increasing interest for solving optimal control problems because the characteristics of the orthogonal polynomials are very well suited to the mathematical operations re-

quired to solve the optimal control problem: functions can be very accurately approximated, derivatives of the state functions at the nodes are computed by matrix multiplication only and any integral associated with the problem is approximated using well-known Gauss quadrature rules. This, together with the fact that pseudospectral methods have a rapid rate of convergence (i.e. convergence to a very accurate solution with few number of nodes), is the reason for using pseudospectral methods in this work.

Here, a particular implementation of a direct pseudospectral method is chosen: PSOPT, see (Becerra, 2010). PSOPT is an open source tool developed by Victor M. Becerra of the University of Reading and is written in C++ and is interfaced to IPOPT (Interior Point OPTimizer) (Wächter and Biegler, 2006) to solve the NLP problem. PSOPT can deal with all optimal control problem elements defined above: multi-phase problems, phase linkage constraints, boundary constraints, path constraints, static optimisation parameters and bounds on state variables, control variables and time.

4. First guess transfers

In order to initialise the optimisation, PSOPT requires a first guess. Here, first guesses for each of the transfer cases are generated using the concept of "patched restricted three-body problems approximation" (Mingotti et al., 2011, Mingotti et al., 2014). Important to note is the fact that these first guesses assume a constant attitude of the sail with respect to the Sun-sail line. They are sub-optimal in the sense that minor discontinuities exist in position and velocities at the linkage between the two three-body systems and no fourth body perturbations are considered .The next subsections give a detailed mathematical overview of the patched restricted three-body problems approximation and the resulting first guesses that are transferred into PSOPT to generate optimal transfers in Section 5.

4.1 Definition of solar sail dedicated sets

Let $\mathbf{x}_0$ be a vector representing a generic initial state, $\mathbf{x}_0 = \left(x_0, y_0, z_0, \dot{x}_0, \dot{y}_0, \dot{z}_0\right)$; then let the flow of the dynamical system be $\phi_{\mathbf{u}(\alpha,\delta)}\left(\mathbf{x}_0, t_0; t\right)$ be at time t starting from $\left(\mathbf{x}_0, t_0\right)\big|$ and considering the control law, based on the exploitation of solar radiation pressure, $\mathbf{u}\left(\alpha,\delta\right) = a_s\hat{\mathbf{n}}\left(t\right), t\left[t_0, t_f\right]$. With this notation, it is possible to define the generic point of a solar sail trajectory through

$$\mathbf{x}\left(t\right) = \phi_{\bar{\mathbf{u}}(\alpha,\delta)}\left(\mathbf{x}_0, t_0; t\right) \tag{19}$$

where $\bar{\mathbf{u}}(\alpha,\delta)$ is the control vector assuming that the solar sail remains at a fixed attitude with respect to the Sun-sail line, i.e. with constant cone angle α and constant clock angle δ, see Figure 1b.

Let $\mathrm{P}(\varepsilon)$ and $\mathrm{Q}(\theta)$ be two surfaces of section perpendicular to the $(\mathrm{x},\mathrm{y})-$plane: the first one is perpendicular to the $\mathrm{x}-$axis and is located at a distance ε (along the $\mathrm{x}-$axis) from the rotating frame origin, while the second one forms an angle θ with the $\mathrm{x}-$axis.

The solar sail orbit, for chosen values of ε and θ, is

$$\gamma_{\bar{\mathbf{u}}(\alpha,\delta)}(\mathbf{x}_0,\tau,\varepsilon,\theta)=\left\{\phi_{\bar{\mathbf{u}}(\alpha,\delta)}(\mathbf{x}_0,\mathrm{t}_0;\tau)\,|\,0\le\tau\le\mathrm{t}_\mathrm{Q}-\mathrm{t}_\mathrm{P}\right\} \tag{20}$$

where the dependence on the initial state $\mathbf{x}_0$ is kept. In Eq. (20), τ is the duration of the solar sail contribution, whereas t_P and t_Q are the time at which the orbit intersects $\mathrm{P}(\varepsilon)$ (for the first time) and $\mathrm{Q}(\theta)$, respectively. Assuming the orbit crosses section $\mathrm{P}(\varepsilon)$ before $\mathrm{Q}(\theta)$, i.e. $\mathrm{t}_\mathrm{P}\le\mathrm{t}_\mathrm{Q}$, the solar sail is active (i.e. $\hat{\mathbf{n}}$ is not orthogonal to $\hat{\mathbf{r}}_\mathrm{I}$) only in the $\mathrm{t}\in\left[\mathrm{t}_\mathrm{P},\mathrm{t}_\mathrm{Q}\right]$ time interval.

The solar sail dedicated set is a collection of solar sail orbits (all computed with the same guidance law $\bar{\mathbf{u}}(\alpha,\delta)$) till they reach the surface $\mathrm{Q}(\theta)$:

$$\mathrm{S}_{\bar{\mathbf{u}}(\alpha,\delta)}(\tau,\varepsilon,\theta)=\bigcup_{\mathbf{x}_0\in\Xi}\gamma_{\bar{\mathbf{u}}(\alpha,\delta)}(\mathbf{x}_0,\tau,\varepsilon,\theta) \tag{21}$$

According to the definition in Eq. (21), the solar sail dedicated set is made up by orbits that reach $\mathrm{Q}(\theta)$ at different times, although all orbits have the same solar sail constant attitude. The cut, in the phase space, of the solar sail dedicate set with the surface $\mathrm{Q}(\theta)$ is named $\partial\mathrm{S}_{\bar{\mathbf{u}}(\alpha,\delta)}(\tau,\varepsilon,\theta)$.

The solar sail dedicated set in Eq . (21) is associated to a generic domain of admissible initial conditions Ξ; it will be shown in the following how Ξ can be defined for solar sail departure and arrival sets, from and to selected periodic orbits, respectively. Thanks to the definition of $\mathrm{S}_{\bar{\mathbf{u}}(\alpha,\delta)}(\tau,\varepsilon,\theta)$, the solar sail acceleration can be incorporated in a three-body frame using the same methodology developed for the invariant manifolds. More specifically, invariant manifolds and solar sail trajectories are replaced by dedicated sets which are manipulated to find connection points on suitable surfaces of section. The idea is to reproduce the role acted by invariant manifolds.

4.2 Solar sail departure sets

The initial state of the transfers, $\mathbf{x}_0$, can be any point that belongs to the selected LPOs of Figure 4a and c, slightly perturbed along the direction of the unstable eigenvector of the periodic orbit monodromy matrix. Therefore, the initial point is the generic departing point

$$\mathbf{x}_0 = \mathbf{x}_0\left(\tau_{\mathrm{O}}^{\mathrm{D}}\right) = \phi\left(\mathbf{x}_{\mathrm{O}}^{\mathrm{D}}, 0; \tau_{\mathrm{O}}^{\mathrm{D}}\right) \pm \varepsilon \mathbf{v}_{\mathrm{u}} \tag{22}$$

and is found by flowing the initial nominal point $\mathbf{x}_{\mathrm{O}}^{\mathrm{D}}$ for a time $\tau_{\mathrm{O}}^{\mathrm{D}} \le \mathrm{P}_{\mathrm{O}}^{\mathrm{D}}$, P_{O} being the initial orbit period and adding the small perturbation $\varepsilon = 1.0 \times 10^{-6}$ along the unstable eigenvector $\mathbf{v}_{\mathrm{s}}$ (the $\pm$ ambiguity is solved by choosing $+$ to generate the exterior branch of the L_2-region manifold for the Earth-L_2 to Mars-L_1 transfer and $-$ to generate the interior branch of the L_1-region manifold for the Earth-L_1 to Mercury-L_1 transfer). The subscript $(\cdot)_{\mathrm{O}}$ stands for the specific departure LPO selected.

The domain of admissible initial states is then written as follows

$$\Xi^{\mathrm{D}} = \left\{ \mathbf{x}_0\left(\tau_{\mathrm{O}}^{\mathrm{D}}\right) \mid \tau_{\mathrm{O}}^{\mathrm{D}} \in \left[0, \mathrm{P}_{\mathrm{O}}^{\mathrm{D}}\right] \right\} \tag{23}$$

and the periodic orbit solar sail departure set, for some $\alpha_{\mathrm{D}} \neq 90$ deg, $\tau_{\mathrm{D}} > 0$, is given by the forward integration

$$\mathrm{D}^{\mathrm{O}}_{\bar{\mathbf{u}}(\alpha_{\mathrm{D}}, \delta_{\mathrm{D}})}\left(\tau_{\mathrm{D}}, \varepsilon_{\mathrm{D}}, \theta_{\mathrm{D}}\right) = \bigcup_{\mathbf{x}_0 \in \Xi^{\mathrm{D}}} \gamma_{\bar{\mathbf{u}}(\alpha_{\mathrm{D}}, \delta_{\mathrm{D}})}\left(\mathbf{x}_0, \tau_{\mathrm{D}}, \varepsilon_{\mathrm{D}}, \theta_{\mathrm{D}}\right) \tag{24}$$

The superscript $(\cdot)^{\mathrm{O}}$ stands for the specific departure LPO selected.

When the cone angle $\alpha_{\mathrm{D}} = 90$ deg, no solar sail acceleration acts ($\tau_{\mathrm{D}} = 0$) and the classic unstable manifolds of the relative LPOs are found as $\mathrm{W}^{\mathrm{O}}_{\bar{\boldsymbol{\theta}}(90, \delta_{\mathrm{D}})}\left(0, \varepsilon_{\mathrm{D}}, \theta_{\mathrm{D}}\right)$, directly following from Eq. (24). The cut, in the phase space, of the periodic orbit solar sail departure set with the surface $\mathrm{Q}_{\mathrm{D}}\left(\theta_{\mathrm{D}}\right)$ is named $\partial \mathrm{D}^{\mathrm{O}}_{\bar{\mathbf{u}}(\alpha_{\mathrm{D}}, \delta_{\mathrm{D}})}\left(\tau_{\mathrm{D}}, \varepsilon_{\mathrm{D}}, \theta_{\mathrm{D}}\right)$, while the cut of the set describing the classic unstable manifold trajectories is named $\partial \mathrm{W}^{\mathrm{O}}_{\bar{\boldsymbol{\theta}}(90, \delta_{\mathrm{D}})}\left(0, \varepsilon_{\mathrm{D}}, \theta_{\mathrm{D}}\right)$.

4.3 Solar sail arrival sets

Very similar to the solar sail departure sets, the solar sail arrival sets can be derived: the final state of the transfers, $\mathbf{x}_{\mathrm{f}}$, can be any point that belongs to the selected LPOs Figure 4b and d,

slightly perturbed along the direction of the stable eigenvector of the periodic orbit monodromy matrix. Therefore, the final point is the generic insertion point

$$\mathbf{x}_{\mathrm{f}} = \mathbf{x}_{\mathrm{f}}\left(\tau_{\mathrm{O}}^{\mathrm{A}}\right) = \phi\left(\mathbf{x}_{\mathrm{O}}^{\mathrm{A}}, 0; \tau_{\mathrm{O}}^{\mathrm{A}}\right) \pm \varepsilon \mathbf{v}_{\mathrm{s}} \tag{25}$$

and is found by flowing the initial nominal point $\mathbf{x}_{\mathrm{O}}^{\mathrm{A}}$ for a time $\tau_{\mathrm{O}}^{\mathrm{A}} \le \mathrm{P}_{\mathrm{O}}^{\mathrm{A}}$, $\mathrm{P}_{\mathrm{O}}^{\mathrm{A}}$ being the final orbit period and adding the small perturbation $\varepsilon = 1.0 \times 10^{-6}$ along the stable eigenvector $\mathbf{v}_{\mathrm{s}}$ (in this case, the $\pm$ ambiguity is solved by choosing $+$ to generate the exterior branch of the L_2-region manifold for the Earth-L_1 to Mercury-L_2 transfer and $-$ to generate the interior branch of the L_1-region manifold for the Earth-L_2 to Mars-L_1 transfer). The subscript $(\cdot)_{\mathrm{O}}$ stands for the specific arrival LPO selected.

The domain of admissible final states is then written as follows

$$\Xi^{\mathrm{A}} = \left\{ \mathbf{x}_{\mathrm{f}}\left(\tau_{\mathrm{O}}^{\mathrm{A}}\right) \mid \tau_{\mathrm{O}}^{\mathrm{A}} \in \left[0, \mathrm{P}_{\mathrm{O}}^{\mathrm{A}}\right] \right\} \tag{26}$$

and the periodic orbit solar sail arrival set, for some $\alpha_{\mathrm{A}} \neq 90$ deg, $\tau_{\mathrm{A}} > 0$, is given by the backward integration

$$\mathrm{A}^{\mathrm{O}}_{\bar{\mathbf{u}}(\alpha_{\mathrm{A}}, \delta_{\mathrm{A}})}\left(\tau_{\mathrm{A}}, \varepsilon_{\mathrm{A}}, \theta_{\mathrm{A}}\right) = \bigcup_{\mathbf{x}_{\mathrm{f}} \in \Xi^{\mathrm{A}}} \gamma_{\bar{\mathbf{u}}(\alpha_{\mathrm{A}}, \delta_{\mathrm{A}})}\left(\mathbf{x}_{\mathrm{f}}, -\tau_{\mathrm{A}}, \varepsilon_{\mathrm{A}}, \theta_{\mathrm{A}}\right) \tag{27}$$

The superscript $(\cdot)^{\mathrm{O}}$ stands for the specific arrival LPO selected.

Similarly as for the departure sets, when the cone angle $\alpha_{\mathrm{A}} = 90$ deg, no solar sail acceleration acts ($\tau_{\mathrm{A}} = 0$) and the classic stable manifolds of the relative LPOs are found as $\mathrm{W}^{\mathrm{O}}_{\bar{\mathbf{0}}(90, \delta_{\mathrm{A}})}\left(-0, \varepsilon_{\mathrm{A}}, \theta_{\mathrm{A}}\right)$, directly following from Eq. (27). The cut, in the phase space, of the periodic orbit solar sail arrival set with the surface $\mathrm{Q}_{\mathrm{A}}\left(\theta_{\mathrm{A}}\right)$ is named $\partial \mathrm{A}^{\mathrm{O}}_{\bar{\mathbf{u}}(\alpha_{\mathrm{A}}, \delta_{\mathrm{A}})}\left(-\tau_{\mathrm{A}}, \varepsilon_{\mathrm{A}}, \theta_{\mathrm{A}}\right)$, while the cut of the set describing the classic stable manifold trajectories is named $\partial \mathrm{W}^{\mathrm{O}}_{\bar{\mathbf{0}}(90, \delta_{\mathrm{A}})}\left(-0, \varepsilon_{\mathrm{A}}, \theta_{\mathrm{A}}\right)$.

4.4 First guess design technique

The key idea to generate the first guess solutions is to replace invariant manifolds with solar sail dedicated sets, and to manipulate the latter in the same way manifolds are used to design space transfers (Mingotti et al., 2011, Mingotti et al., 2014). With the inclusion of the solar sail acceleration and keeping the attitude of the solar sail constant - throughout the complete transfer - with respect to the Sun-sail line, intersections between restricted three-body models can be found

on suitable Poincaré sections, also for the Earth-L_2 to Mars-L_1 and the Earth-L_1 to Mercury-L_2 transfers. Therefore, the propellant-free feature of solar sails is combined with the exploitation of the n-body problems' intrinsic dynamics with a view of generating efficient trajectories. In detail, the technique to build first guesses, with the introduction of a few design variables, is split into the following basic phases.

i. The initial state of the transfer, as defined in Eq. (22), is propagated forward until it intersects a suitable Poincaré surface of section $\mathrm{Q_D}(\theta_\mathrm{D})$, after crossing a previous section $\mathrm{P_D}(\varepsilon_\mathrm{D})$; as already described, the solar sail control is allowed (i.e. the sail is active) only between these two surfaces. If the trajectory is purely ballistic, it moves along the unstable manifold of the selected LPO, i.e. on $\mathrm{W}^{\mathrm{O}}_{\bar{\mathbf{0}}(90,\delta_\mathrm{D})}(0,\varepsilon_\mathrm{D},\theta_\mathrm{D})$, otherwise, if solar radiation pressure is actively exploited, it moves along the solar sail periodic orbit departure set $\mathrm{D}^{\mathrm{O}}_{\bar{\mathbf{u}}(\alpha_\mathrm{D},\delta_\mathrm{D})}(\tau_\mathrm{D},\varepsilon_\mathrm{D},\theta_\mathrm{D})$.

ii. The final state of the transfer, as defined in Eq. (25), is propagated backward until it intersects a suitable Poincaré surface of section $\mathrm{Q_A}(\theta_\mathrm{A})$, after crossing a previous section $\mathrm{P_A}(\varepsilon_\mathrm{A})$; as per phase (i), the solar sail control is allowed (i.e. the sail is active) only between these two surfaces. If the trajectory is purely ballistic, it moves along the stable manifold of the selected LPO, i.e. on $\mathrm{W}^{\mathrm{O}}_{\bar{\mathbf{0}}(90,\delta_\mathrm{A})}(-0,\varepsilon_\mathrm{A},\theta_\mathrm{A})$, otherwise, if solar radiation pressure is actively exploited, it moves along the solar sail periodic orbit arrival set $\mathrm{A}^{\mathrm{O}}_{\bar{\mathbf{u}}(\alpha_\mathrm{A},\delta_\mathrm{A})}(-\tau_\mathrm{A},\varepsilon_\mathrm{A},\theta_\mathrm{A})$.

iii. As mentioned in Section 3.1, the dynamical systems under consideration are different for the two legs of the transfers. Therefore, a proper operator T is introduced in order to map states of the arrival dynamical models (Sun-Mars, Sun-Mercury) into the departure one (Sun-Earth). As no fourth body perturbations are considered, the dynamical models are mutually independent and the departure Poincaré section $\mathrm{Q_D}(\theta_\mathrm{D})$ and the arrival one $\mathrm{Q_A}(\theta_\mathrm{A})$ (after the proper transformation) can therefore be arbitrarily superimposed. After this, on the same Sun-Earth suitable Poincaré section $\mathrm{Q}(\theta)$, the transit point between the solar sail departure set (phase (i)) and the arrival one (phase (ii)) is searched for, by wisely tuning the introduced design variables. Finally, being interested in generating first guesses for interplanetary transfers, once the geometry of the transfer is defined by patching to-

gether the two applicable restricted three-body systems, the launch epoch that enables the transfer - in the real ephemeris model - is found by means of a systematic search.

4.5 Earth-L_2 to Mars-L_1 transit point

The procedure described in the previous section is applied to the Earth-L_2 to Mars-L_1 mission scenario, in order to design a sample feasible first guess solution, as a function of the corresponding design variables reported in Table 3.

Figure 7 and Figure 9a and b show the cuts of the unstable manifold trajectories of the Sun-Earth model, namely $\partial W^{\text{NH-L}_2}_{\bar{\mathbf{0}}(90,\delta_D)}(0,\varepsilon_D,\theta_D)$, and of the solar sail departure dedicated set $\partial D^{\text{NH-L}_2}_{\bar{\mathbf{u}}(\alpha_D,\delta_D)}(\tau_D,\varepsilon_D,\theta_D)$, for the initial northern Halo orbit around Earth-L_2, on suitable Poincaré sections. Moreover, on the same suitable Poincaré sections, Figure 9a and b present the cuts of the stable manifold trajectories of the Sun-Mars model $\partial W^{\text{NH-L}_1}_{\bar{\mathbf{0}}(90,\delta_A)}(-0,\varepsilon_A,\theta_A)$ and of the solar sail arrival dedicated set $\partial A^{\text{NH-L}_1}_{\bar{\mathbf{u}}(\alpha_A,\delta_A)}(-\tau_A,\varepsilon_A,\theta_A)$, for the final northern Halo orbit around Mars-L_1. The cuts are shown on the $(r,v_r)-$ and $(r,v_t)-$sections, with v_r and v_t the radial and traverse velocities, respectively.

For reasonable transfer times, the ballistic manifold structure of the Sun-Earth and the Sun-Mars models do not intersect, while the solar sail dedicated sets allow a transit point

$$T^{\text{NH-L}_2}_{\text{NH-L}_1} \doteq \partial D^{\text{NH-L}_2}_{\bar{\mathbf{u}}(\alpha_D,\delta_D)}(\tau_D,\varepsilon_D,\theta_D) \cap \partial A^{\text{NH-L}_1}_{\bar{\mathbf{u}}(\alpha_A,\delta_A)}(-\tau_A,\varepsilon_A,\theta_A) \tag{28}$$

In the generation process of the first guess solution (which will be optimised in Section 5 using more sophisticated models), small discontinuities (in the out-of-plane components) can be tolerated when looking for the transit point.

4.6 Earth-L_1 to Mercury-L_2 transit point

Using the same procedure described in the previous section, a feasible first guess solution can be obtained for the Earth-L_1 to Mercury-L_2 transfer, as a function of the corresponding design variables reported in Table 3.

Figure 8 and Figure 9c and d represent the cuts of the unstable manifold trajectories of the Sun-Earth model, $\partial W^{\text{NH-L}_1}_{\bar{\mathbf{0}}(90,\delta_D)}(0,\varepsilon_D,\theta_D)$ and of the solar sail departure dedicated set $\partial D^{\text{NH-L}_1}_{\bar{\mathbf{u}}(\alpha_D,\delta_D)}(\tau_D,\varepsilon_D,\theta_D)$, for the initial northern Halo orbit around L_1, on suitable Poincaré sections. Furthermore, on the same suitable Poincaré sections, Figure 9c and d show the cuts of the stable

manifold trajectories of the Sun-Mercury model $\partial \mathrm{W}^{\mathrm{SH\text{-}L_2}}_{\bar{\mathbf{u}}(90,\delta_\mathrm{A})}(-0,\varepsilon_\mathrm{A},\theta_\mathrm{A})$ and of the solar sail arrival dedicated set $\partial \mathrm{A}^{\mathrm{SH\text{-}L_2}}_{\bar{\mathbf{u}}(\alpha_\mathrm{A},\delta_\mathrm{A})}(-\tau_\mathrm{A},\varepsilon_\mathrm{A},\theta_\mathrm{A})$, for the final southern Halo orbit around L_2.

As expected, the pure ballistic manifolds of the Sun-Earth and the Sun-Mercury models do not intersect, while the solar sail dedicated sets allow a transit point

$$\mathrm{T}^{\mathrm{NH\text{-}L_1}}_{\mathrm{SH\text{-}L_2}} \doteq \partial \mathrm{D}^{\mathrm{NH\text{-}L}}_{\bar{\mathbf{u}}(\alpha_\mathrm{D},\delta_\mathrm{D})}(\tau_\mathrm{D},\varepsilon_\mathrm{D},\theta_\mathrm{D}) \cap \partial \mathrm{A}^{\mathrm{NH\text{-}L_2}}_{\bar{\mathbf{u}}(\alpha_\mathrm{A},\delta_\mathrm{A})}(-\tau_\mathrm{A},\varepsilon_\mathrm{A},\theta_\mathrm{A}) \tag{29}$$

Table 3 Values of the design variables for the generation of first guess transfers

Case	$\tau_\mathrm{O}^\mathrm{D}$	α **, deg**	δ **, deg**	ε_D	θ_D	$\tau_\mathrm{O}^\mathrm{A}$	ε_A	θ_A
Earth-L_2 to Mars-L_1	2.3055	62.50	90	1.0170	-147.5	2.9378	0.9925	-45.0
Earth-L_1 to Mercury-L_2	1.7929	-52.75	90	0.9830	-32.5	0.0306	1.0060	-42.5

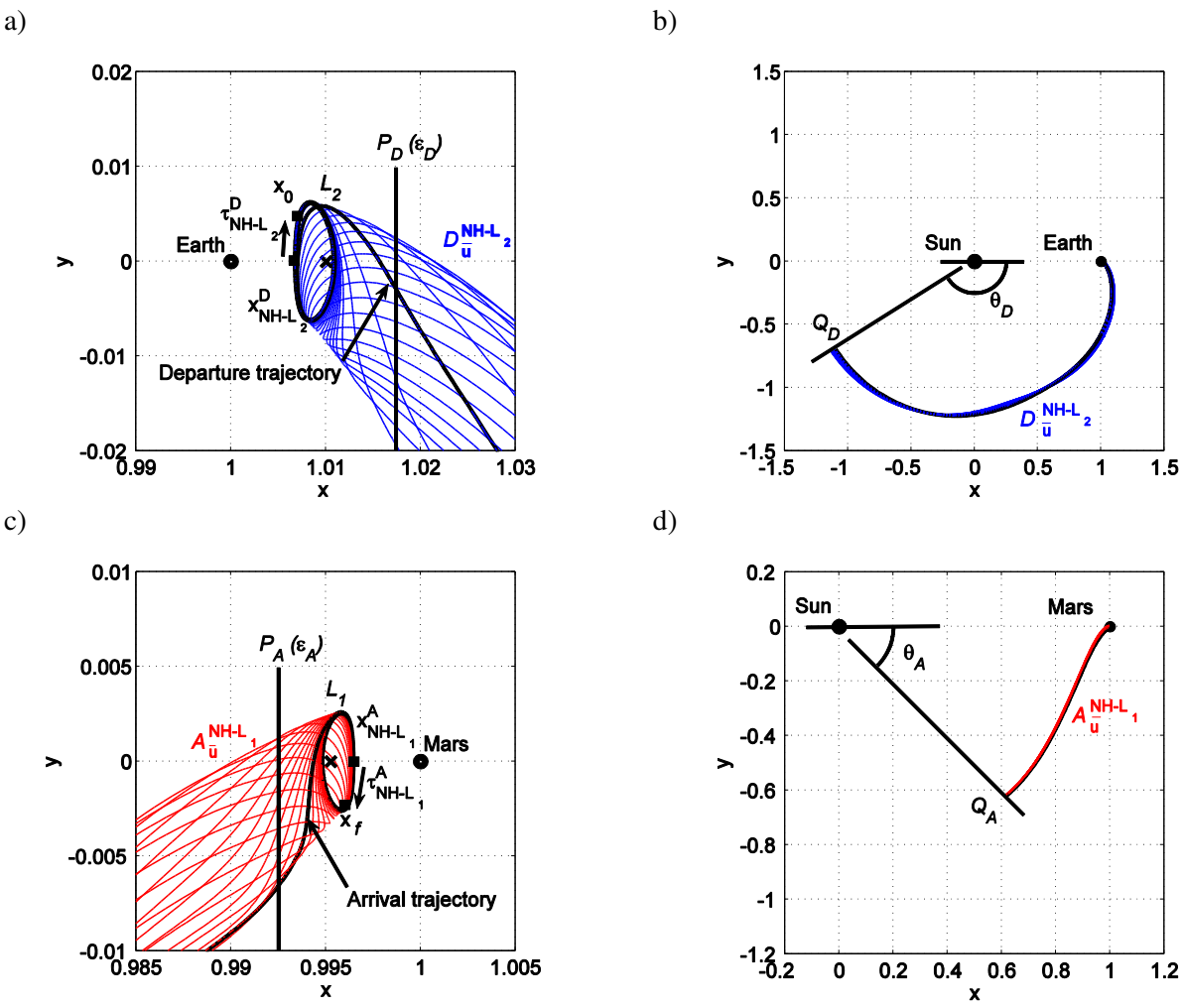

Figure 7 Earth-L_2 to Mars-L_1 first guess transfer. a, b) Departure conditions and design variables. c, d) Arrival conditions and design variables.

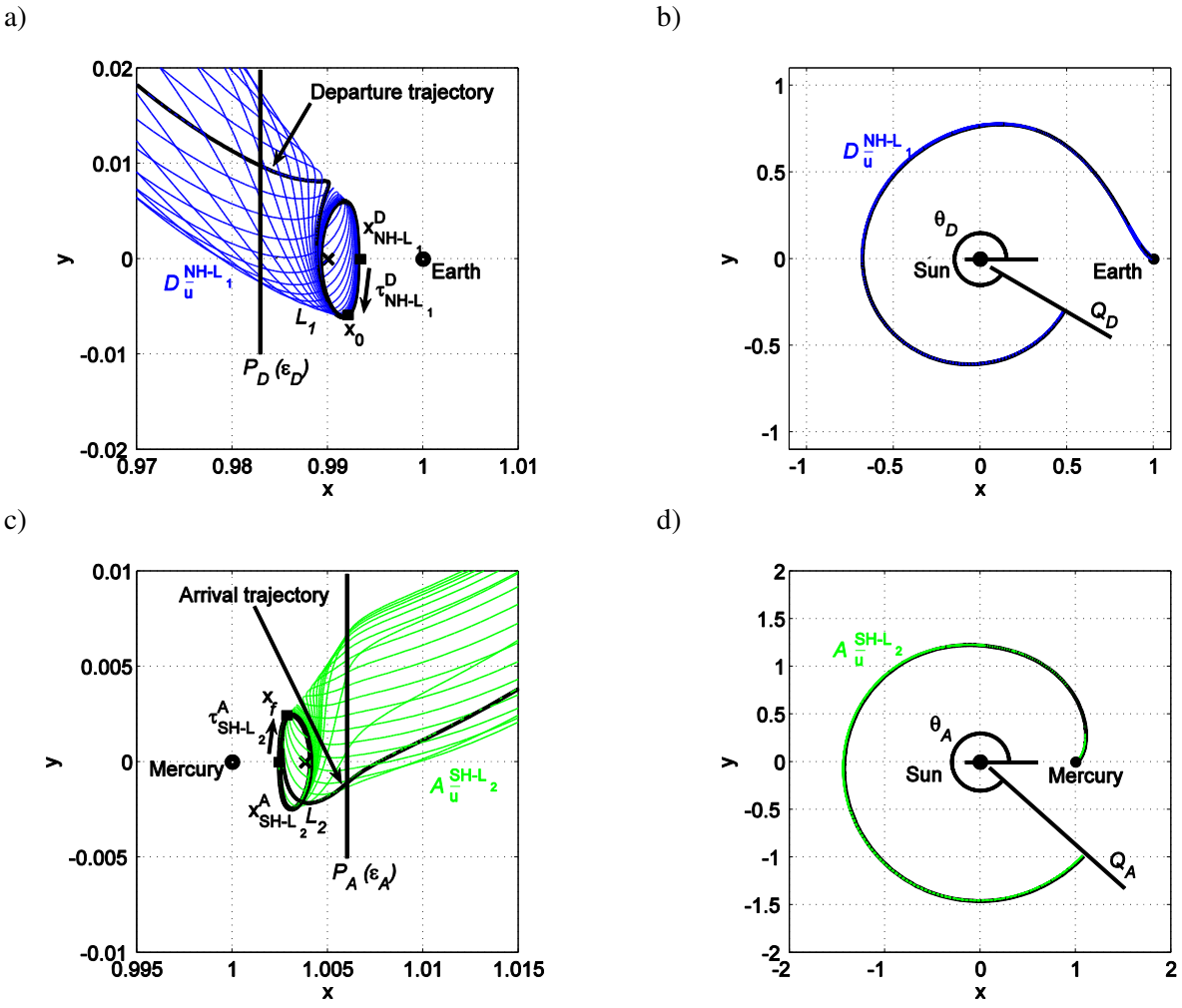

Figure 8 Earth-L_1 to Mercury-L_2 first guess transfers. a, b) Departure conditions and design variables. c, d) Arrival conditions and design variables.

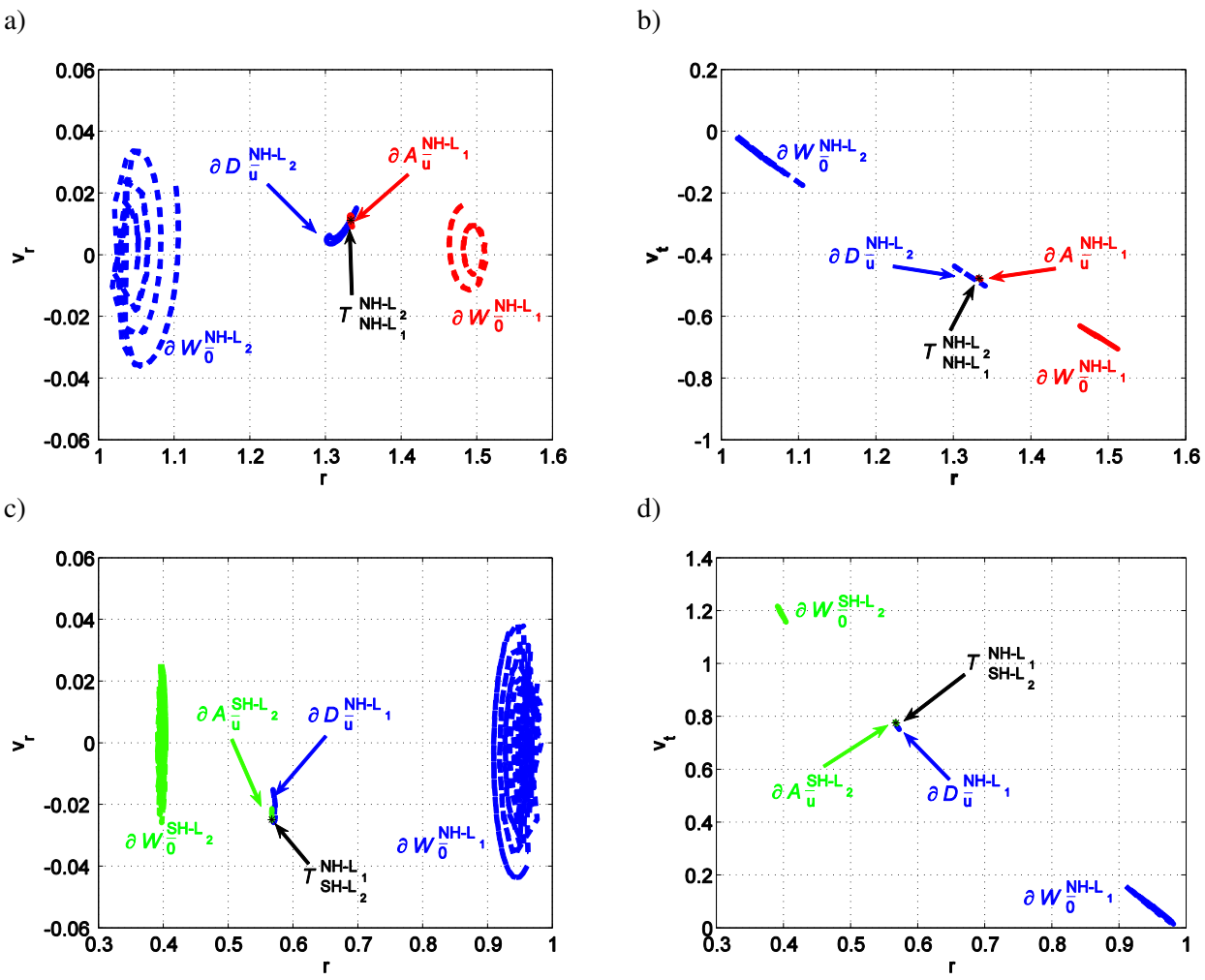

Figure 9 Phase space on suitable Sun-Earth Poincaré sections to design the first guess transfers. a, b) Earth-L_2 to Mars-L_1 scenario. c, d) Earth-L_1 to Mercury-L_2 scenario.

5. Results – Earth-L_2 to Mars-L_1 transfer

Using the first guess designed in the previous section, a range of results for the Earth-L_2 to Mars-L_1 transfer are presented in this section. First, the results for a fully controllable sail are provided, where the constraint in Eq. (18) is omitted. This will provide the absolute minimum time of flight achievable. Subsequently, the constraint in Eq. (18) is introduced and a continuation is started where the results for a larger value for $\Delta\alpha$ are used as a first guess to obtain the results for a smaller value for $\Delta\alpha$. All results consist of 40 collocation points in both phases, i.e. 80 collocation points in total.

Table 4 Earth-L_2 to Mars-L_1 optimal solar sail transfer results

Description	α_{ref} , deg	δ_{ref} , deg	Departure date	Arrival date	Time of flight, days
First guess	n/a	n/a	11/11/2020	11/09/2026	2130
$\Delta\alpha$ inactive	n/a	n/a	01/02/2022	01/08/2024	912
$\Delta\alpha = 20$ deg	34.0	117.3	05/02/2022	06/08/2024	914
$\Delta\alpha = 15$ deg	36.3	109.9	11/02/2022	23/08/2024	924
$\Delta\alpha = 12.5$ deg	35.5	111.3	06/02/2022	27/08/2024	932
$\Delta\alpha = 10$ deg	33.8	116.8	24/01/2022	05/09/2024	955
$\Delta\alpha = 7.5$ deg	35.3	121.3	21/01/2022	03/11/2024	1017

a) b)

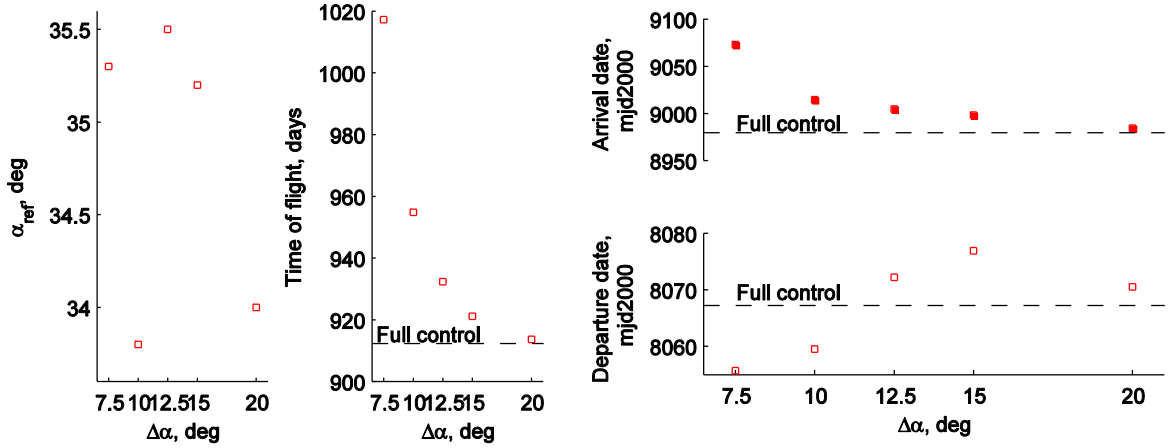

Figure 10 Earth-L_2 to Mars-L_1 optimal solar sail transfer results: influence of solar sail controllability, $\Delta\alpha$. a) Optimal sail reference cone angle and time of flight. c) Departure and arrival dates.

The main results are summarised in Table 4 for both the first guess, the fully controllable solar sail (i.e. $\Delta\alpha$ is inactive) as well as for a range of values for $\Delta\alpha$. Figure 10 presents these results in graphical form to highlight some trends. The smaller the value for $\Delta\alpha$, the more limited the controllability of the sail is. The table clearly demonstrates the effect of this limited controllability as the time of flight increases from 912 days for a fully controllable sail to 1017 days for a very limited steering capability of $\Delta\alpha =$ 7.5 deg. Despite this increase of 11.5 percent, it is remarkable that the transfer can be executed and all constraints can be satisfied with such limited

control capabilities. Note that the significant reduction in the time of flight between the first guess and the fully controllable sail can be attributed to the fact that the first guess considered coasting arcs at the start and end of the transfer while the time-optimal results presented here assume the use of the solar sail from the Earth-L_1 Halo orbit all the way up to the Mars-L_2 Halo orbit. Also note that, compared to previous work by the authors (Heiligers et al., 2014), which considered a simple circular, ecliptic ephemeris for the planets and could therefore produce an optimal transfer for $\Delta\alpha =$ 5.0, the time of flight has increased by 1-2 percent and the achievable minimum value for $\Delta\alpha$ has increased as well. This demonstrates the influence of the true ephemeris (in particular the out-of-ecliptic motion) of the planets.

Details of one particular transfer, i.e. for $\Delta\alpha = 10$ deg are provided in Figure 11. The optimal reference solar sail attitude is indicated with grey arrows in plots a-c, while plot d shows the variation of the cone angle around this optimal reference attitude. The detail in Figure 11b shows where the transfer leaves the Earth-L_2 Halo and where it winds onto the Mars-L_1 Halo. The corresponding values for the optimisation parameters δ_1 and δ_2 are: $\delta_1 =$ 3.0741 and $\delta_2 =$ 1.5765, which closely correspond to the intersections of the Halo orbits with the ecliptic plane. Very similar values for δ_1 and δ_2 are observed for other, small values for $\Delta\alpha$. Finally, in Figure 11e the solar sail acceleration magnitude is provided, which shows an expected decrease when the distance from the Sun becomes larger.

Comparison of the results with results in existing literature is difficult as the literature only considers solar sail orbital rendezvous missions to Mars (Circi, 2004, Mengali and Quarta, 2009, Mengali and Quarta, 2014). In addition, different models are often used for the dynamics, the solar sail acceleration and/or the ephemerides. For example, (Mengali and Quarta, 2009) considered a time-free orbital rendezvous with Mars in a heliocentric two-body model and with circular, ecliptic ephemerides for Earth and Mars. Furthermore, an ideal solar sail model with $a_c = 1$ mm/s^2 (i.e. $\beta = 0.169$) is considered to obtain a minimum time of flight transfer of 408 days with an average cone angle of 44.94 deg for a fully controllable solar sail. Solving the problem considered in this work for a fully controllable solar sail and for $\beta = 0.169$, a minimum time of flight of 384 days is obtained with an average cone angle of 40.6 deg. The shorter time of flight can be attributed to the shorter distance between the start and end of the transfer (i.e. from Halo to Halo rather than from Earth to Mars) as well as the exploitation of the three-body dynamics.

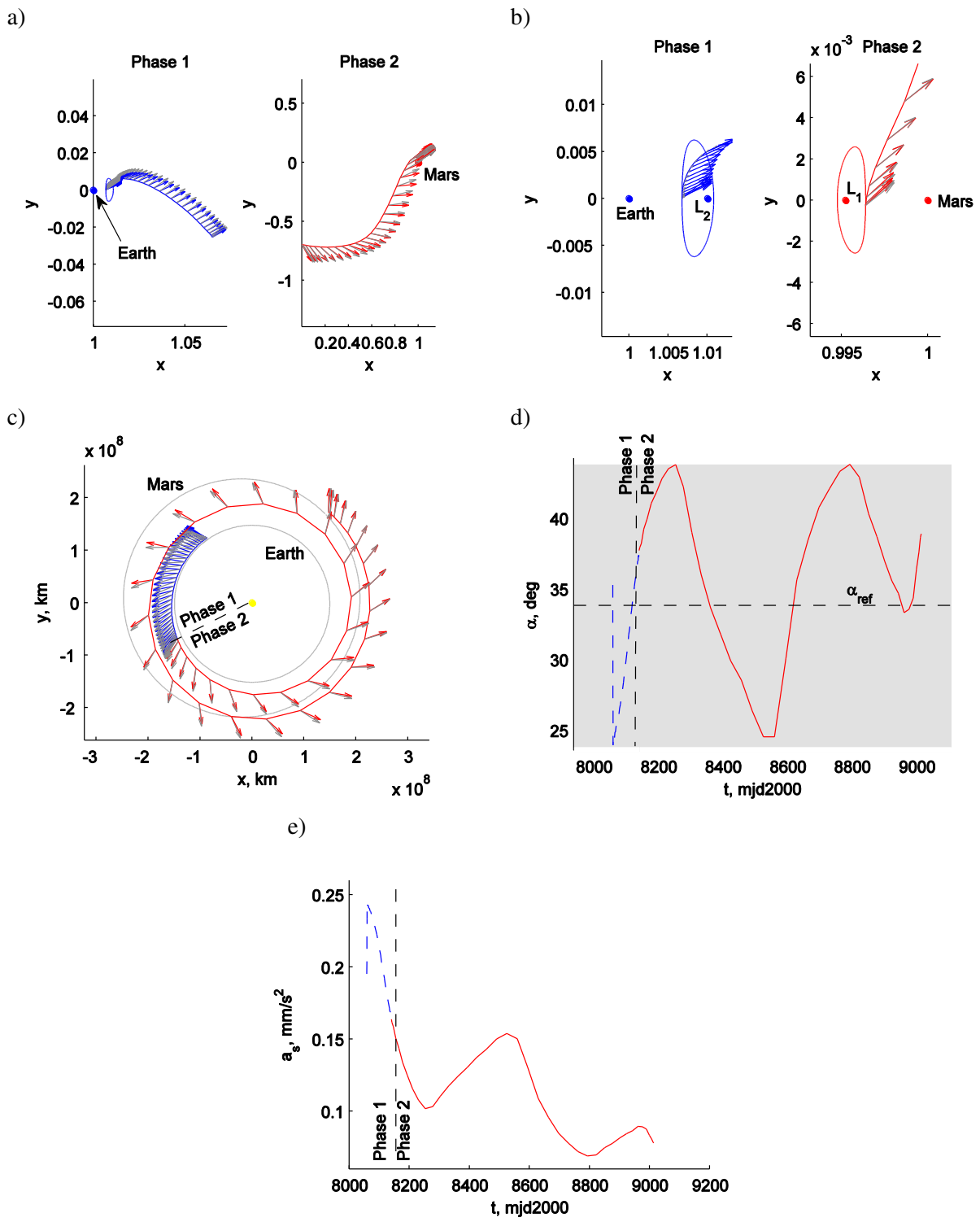

Figure 11 Earth-L_2 to Mars-L_1 solar sail transfer: details for $\Delta\alpha = 10$ deg. a) Transfer phases with sail acceleration direction (color) and optimal $\hat{n}_{ref}$ -direction (grey). b) Detail of plot a). c) Transfer in heliocentric inertial reference frame. d) Cone angle. e) Solar sail acceleration magnitude.

Limitations on the steering capabilities of the solar sail as introduced in this paper are only considered by (Mengali and Quarta, 2014). The authors fix the cone angle of the solar sail and allow only the clock angle to vary. Note that the cone angle restricts the solar sail acceleration vector to a cone around the Sun-sail line and the clock angle determines the location of the sail acceleration vector on this cone, see also Figure 6a. In this case, due to differences in the assumed models (e.g. optical solar sail force model), the minimum time of flight for a fully controllable sail with $a_c = 1$ mm/s^2 ($\beta = 0.169$) is 381 days. The authors then find that a constant cone angle of 43 deg minimises the penalty on the time of flight, which becomes 405 days. It is clear that a constant cone angle of 43 deg and a clock angle variation between $-\pi$ and π still provides much more control capabilities to the sail than the restrictions imposed in this work: for $\beta = 0.169$ and $\Delta\alpha = 7.5$ deg the time of flight increases from 384 days to 518 days. Interestingly, this is a much larger percentage increase (35 percent) than for a sail performance of $\beta =$ 0.05 as considered in Table 4 and Figure 10 (only 11.5 percent). It therefore seems that, the better the sail performance, the larger the negative impact on the trajectory performance when limitations on the sail steering capabilities are introduced.

6. Results – Earth-L_1 to Mercury-L_2 transfer

The optimal results for the Earth-L_1 to Mercury-L_2 transfer are presented in a similar way as for the Earth-L_2 to Mars-L_1 transfer: Table 5 provides departure and arrival dates and time of flight for the first guess, the fully controllable solar sail and for different values for $\Delta\alpha$. It also contains the optimal reference attitude of the solar sail, through α_{ref} and δ_{ref}. Figure 12 provides similar information in graphical form, while Figure 13 shows details of the transfer with $\Delta\alpha =$ 20.0 deg.

Very similar conclusions as for the Earth-Mars transfer can be drawn for the Earth-Mercury transfer: the smaller the value for $\Delta\alpha$, the larger the time of flight and in this case also the smaller the value for α_{ref}. Considering the penalty on the time of flight for decreasing $\Delta\alpha$, for a fully controllable solar sail the time of flight is 808 days, which increases to 936 days for $\Delta\alpha =$ 7.5 deg, which is an increase of 15.8 percent. Again, compared to previous work by the authors where a circular, elliptic ephemeris was assumed, the time of flights have increased by 6 percent (full control) and 22.5 percent ($\Delta\alpha = 7.5$ deg). Furthermore, while the circular, elliptic ephemeris allowed values for $\Delta\alpha$ down to 2.5 deg, the current results show a minimum value for $\Delta\alpha$ of 7.5

deg. With the inclination of Mercury much greater than for Mars such results were expected and again clearly show the influence of the true ephemeris of the planets.

Table 5 Earth-L_1 to Mercury-L_2 solar sail transfer results

Description	α_{ref} , deg	δ_{ref} , deg	Departure date	Arrival date	Time of flight, days
First guess	n/a	n/a	02/10/2020	30/03/2024	1269.4
$\Delta\alpha$ inactive	n/a	n/a	04/09/2021	21/11/2023	808
$\Delta\alpha = 20$ deg	-32.5	86.6	01/09/2021	19/11/2023	809
$\Delta\alpha = 15$ deg	-32.0	86.9	20/08/2021	16/11/2023	817
$\Delta\alpha = 12.5$ deg	-29.6	86.9	26/07/2021	14/11/2023	841
$\Delta\alpha = 10$ deg	-23.4	102.7	22/06/2021	21/12/2023	913
$\Delta\alpha = 7.5$ deg	-22.9	103.7	04/06/2021	28/12/2023	936

a) b)

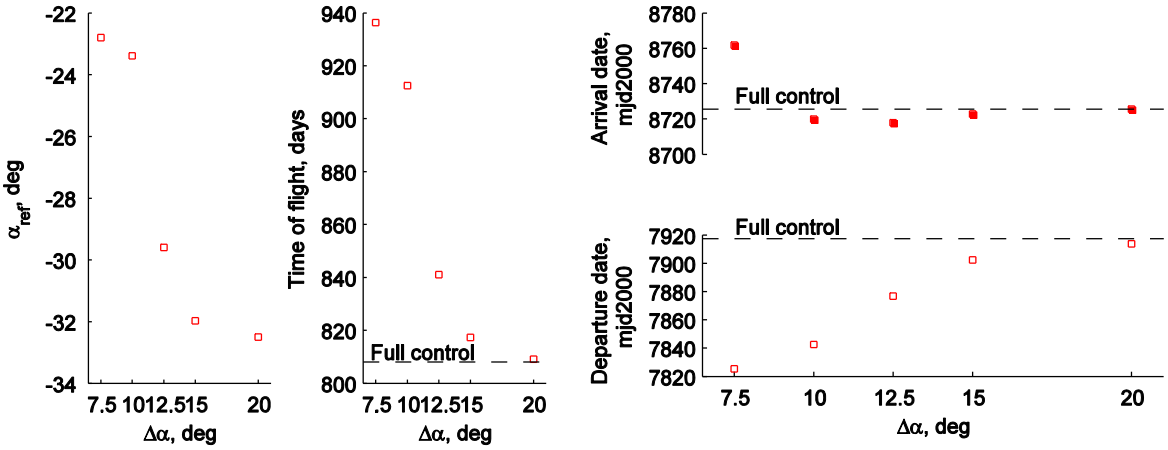

Figure 12 Earth-L_1 to Mercury-L_2 optimal solar sail transfer results: influence of solar sail controllability, $\Delta\alpha$. a) Optimal sail reference cone angle and time of flight. b) Departure and arrival dates.

A comparison with existing results in the literature is again difficult due to differences in dynamical and solar sail models and ephemerides. However, (Quarta and Mengali, 2008) do provide a minimum time of flight for the fully controllable sail between co-planar circular Earth and Mercury orbits. However, an optical sail model and an orbital rendezvous rather than a transfer between LPOs of different CR3BP is considered. The result by (Quarta and Mengali, 2008) for a characteristic sail acceleration of 0.3 mm/s^2 is 2.4 years or approximately 875 days, which is comparable to a transfer with $\Delta\alpha$ = 10-12.5 deg in Table 5.

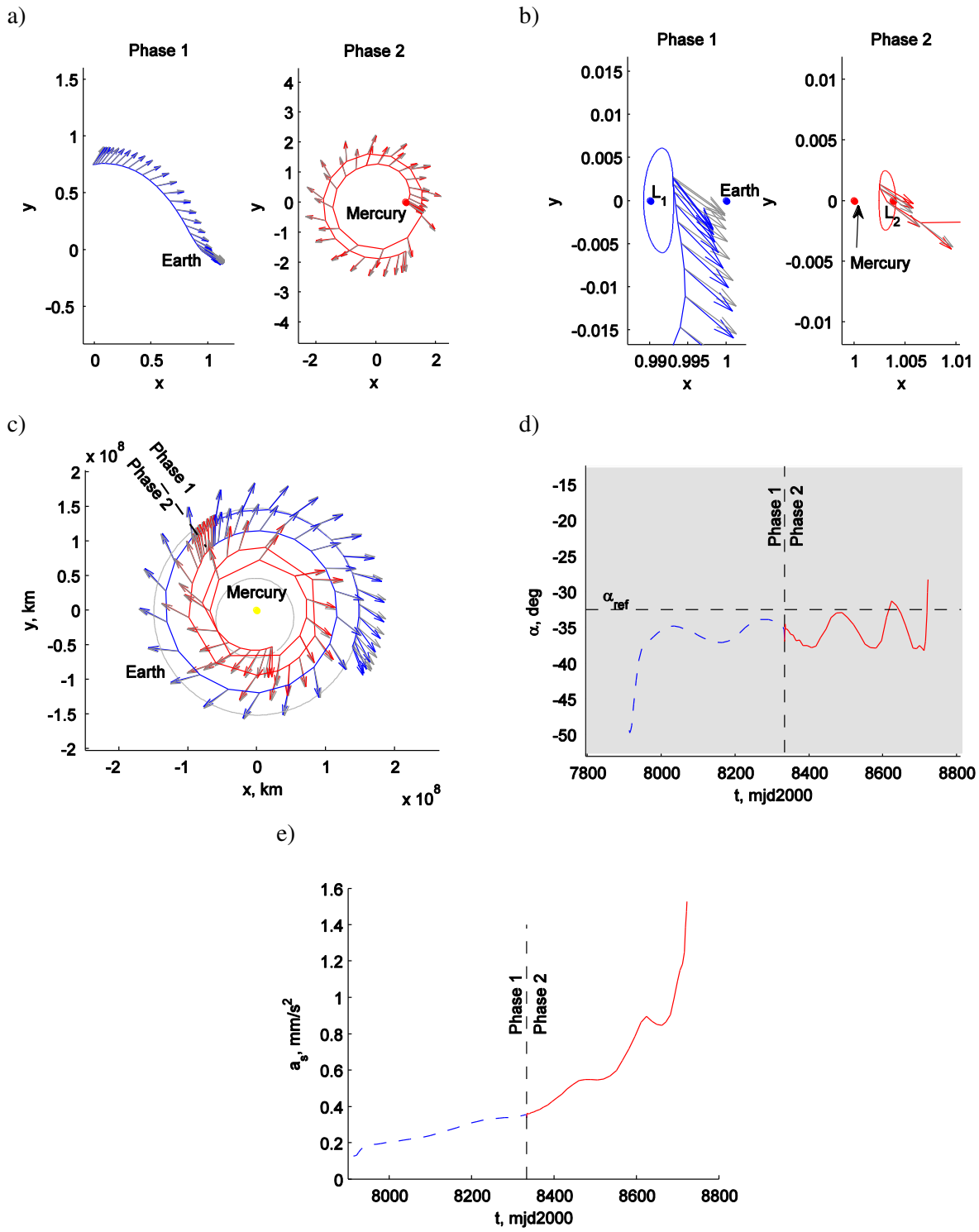

Figure 13 Earth-L_1 to Mercury-L_2 optimal solar sail transfer: details for $\Delta\alpha = 20$ deg. a) Transfer phases with sail acceleration direction (color) and optimal $\hat{\mathbf{n}}_{ref}$ -direction (grey). b) Detail of plot a). c) Transfer in heliocentric inertial reference frame. d) Cone angle. e) Solar sail acceleration magnitude.

Conclusions

In this paper, optimal solar sail trajectories between Libration Point Orbits (LPOs) of different restricted Sun-planet three-body systems have been investigated. Two transfers have been considered in particular: 1) from a Sun-Earth L_2-Halo orbit to a Sun-Mars L_1-Halo orbit and 2) from a Sun-Earth L_1-Halo orbit to a Sun-Mercury L_2-Halo orbit. In addition, the paper has focused on finding transfers that are achievable both with fully controllable solar sails as well as with low-control authority solar sails (mimicking the capabilities of SpaceChips). In all cases, the objective has been to minimise the time of flight. To that end, the optimal control problem has been derived and solved with a particular implementation of a direct pseudospectral method, PSOPT. A two-phase approach has been adopted in order to model the start of the transfer in one Sun-planet CR3BP and the end of the transfer in another Sun-planet CR3BP (including fourth-body perturbations). These phases are linked in terms of state, control and time in inertial space considering the true ephemerides of the planets involved. The case of low-control authority solar sails is modeled by defining a cone of half-angle $\Delta\alpha$ around a to-be optimised sail reference attitude. The results show that, for a sail performance comparable to that of NASA's Sunjammer sail, the Earth-Mars and Earth-Mercury transfers can be performed with little steering effort as $\Delta\alpha$ can be as small as 7.5 deg. Compared to a fully controllable solar sail, the penalty on the time of flight is modest: for the Earth-Mars transfer, the transfer times are 912 days (full control) and 1017 days ($\Delta\alpha = 7.5$ deg), while for the Earth-Mercury transfer, the transfer times are 808 days (full control) and 936 days ($\Delta\alpha = 7.5$ deg), all within a 2020-2025 launch window and 2020-2027 arrival window. By demonstrating the feasibility of these two particular transfers, the results of this point design approach can serve as a basis for the examination of entire families of solutions between a range of LPOs in different Sun-planet systems.

Acknowledgements

This work was funded by the European Research Council Advanced Investigator Grant-227571: Visionary Space Systems - Orbital Dynamics at Extremes of Spacecraft Length-Scale.

References

Baig, S. and McInnes, C. R.. Light-Levitated Geostationary Cylindrical Orbits Are Feasible. J. Guid. Control Dynam., 33**,** 782-793, doi. 10.2514/1.46681. 2010.

Baoyin, H. and McInnes, C.. Solar Sail Halo Orbits at the Sun-Earth Artificial L1-point. Celest. Mech. Dyn. Astron., 94**,** 155-171, doi. 10.1007/s10569-005-4626-3. 2006.

Battin, R. H.. An Introduction to the Mathematics and Methods of Astrodynamics, Revised Edition, Reston, USA, American Institute of Aeronautics and Astronautics, Inc. 2009

Becerra, V. M. Solving Complex Optimal Control Problems at No Cost with PSOPT. IEEE Multi-conference on Systems and Control, 7-10 September 2010 Yokohama, Japan. 2010

Circi, C.. Mars and Mercury Missions Using Solar Sails and Solar Electric Propulsion. J. Guid. Control Dynam., 27**,** 496-498, doi. 10.2514/1.5425. 2004

Colombo, C., Lucking, C. and McInnes, C.. Orbital dynamics of high area-to-mass ratio spacecraft with J2 and solar radiation pressure for novel Earth observation and communication services. Acta Astronaut., 81**,** 137-150, doi. 10.1016/j.actaastro.2012.07.009. 2012.

Dysli, P.. Analytical Ephemeris for Planets (MATLAB code uplanet.m). 1977

Heiligers, J., Ceriotti, M., McInnes, C. R. and Biggs, J. D.. Displaced Geostationary Orbit Design Using Hybrid Sail Propulsion. J. Guid. Control Dynam., 34**,** 1852-1866, doi. 10.2514/1.53807. 2011

Heiligers, J., Ceriotti, M. and McInnes, C. R.. Hybrid low-thrust transfers to eight-shaped orbits for polar observation (IAC-12-C.1.4.2). 63rd International Astronautical Congress. Naples, Italy. 2012

Heiligers, J., Diedrich, B., Derbes, B. and McInnes, C. R.. Sunjammer: Preliminary End-to-End Mission Design. 2014 AIAA/AAS Astrodynamics Specialist Conference. San Diego, CA, USA. 2014.

Heiligers, J. and McInnes, C. R.. Agile Solar Sailing in Three-body Problem: Motion Between Artificial Equilibrium Points (IAC-13-C1.8.3). 64th International Astronautical Congress. Beijing, China. 2013

Heiligers, J., Mingotti, G. and McInnes, C. R.. Optimisation of Solar Sail Interplanetary Heteroclinic Connections. 2nd IAA Conference on Dynamics and Control of Space Systems. Rome, Italy. 2014.

Howell, K. C.. Three-Dimensional, Periodic, 'Halo' Orbits. Celest. Mech. Dyn. Astron., 32**,** 53-71, doi. 10.1007/BF01358403. 1983

McInnes, C. R.. Solar Sail Trajectories at the Lunar L2 Lagrange Point. J. Spacecraft Rockets, 30**,** 782-784, doi. 10.2514/3.26393. 1993.

McInnes, C. R.. Solar Sailing: Technology, Dynamics and Mission Applications, Berlin, Springer-Praxis Books in Astronautical Engineering, Springer-Verlag. 1999.

Mengali, G. and Quarta, A. A.. Solar Sail Trajectories with Piecewise-Constant Steering Laws. Aerospace Science and Technology, 13**,** 431-441, doi. 10.1016/j.ast.2009.06.007. 2009.

Mengali, G. and Quarta, A. A.. Optimal Solar Sail Interplanetary Trajectories with Constant Cone Angle. Advances in Solar Sailing. Berlin: Springer-Praxis Books in Astronautical Engineering, Springer-Verlag. 2014.

Mingotti, G., Heiligers, J. and McInnes, C. R.. First-Guess Generation of Solar Sail Interplanetary Heteroclinic Connections. 2nd IAA Conference on Dynamics and Control of Space Systems. Rome, Italy. 2014.

Mingotti, G., Sanchez, J., McInnes, C.. Combined low-thrust propulsion and invariant manifold trajectories to capture NEOs in the Sun-Earth circular restricted three-body problem. Celest. Mech. Dyn. Astron., 120, 309-336, doi. 10.1007/s10569-014-9589-9. 2014.

Mingotti, G., Topputo, F. and Bernelli-Zazzera, F.. Earth–Mars transfers with ballistic escape and low-thrust capture. Celest. Mech. Dyn. Astron., 110**,** 169-188, doi. 10.1007/s10569-011-9343-5. 2011.

Pergola, P., Geurts, K., Casaregola, C. and Andrenucci, M.. Earth-Mars Halo to Halo Low Thrust Manifold Transfers. Celest. Mech. Dyn. Astron., 105**,** 19-32, doi. 10.1007/s10569-009-9205-6. 2009.

Quarta, A. A. and Mengali, G.. Solar Sail Missions to Mercury with Venus Gravity Assist. Acta Astronaut., 65**,** 495-506, doi. 10.1016/j.actaastro.2009.02.007. 2008.

Topputo, F., Vasile, M. and Bernelli-Zazzera, F.. Low Energy Interplanetary Transfers Exploiting Invariant Manifolds of the Restricted Three-Body Problem. Journal of the Astronautical Sciences, 53**,** 353-372. 2005.

Tsuda, Y., Mori, O., Funase, R., Sawada, H., Yamamoto, T., Saiki, T., Endo, T. and Kawaguchi, J.. Flight Status of IKAROS Deep Space Solar Sail Demonstrator. Acta Astronaut., 69**,** 833-840, doi. 10.1016/j.actaastro.2011.06.005. 2011.

Wächter, A. and Biegler, L. T.. On the Implementation of an Interior-point Filter Line-search Algorithm for Large-scale Nonlinear Programming. Mathematical Programming, 106**,** 25-57, doi. 10.1007/s10107-004-0559-y. 2006.

Wawrzyniak, G. G. and Howell, K. C.. Investigating the Design Space for Solar Sail Trajectories in the Earth-Moon System. The Open Aerospace Engineering Journal, 4**,** 26-44. 2011.